

Helicopter-borne and ground-towed radar surveys of the Fourcade Glacier on King George Island, Antarctica

K. Y. Kim^{1,4} J. Lee² M. H. Hong¹ J. K. Hong² H. Shon³

¹Department of Geophysics, Kangwon National University, Chunchon, 200-701, Korea.

²Korea Polar Research Institute, Incheon P.O. Box 32, 406-840, Korea.

³Department of Civil, Environmental and Railroad Engineering, Pai Chai University, Daejeon 302-735, Korea.

⁴Corresponding author. Email: kykim@kangwon.ac.kr

Abstract. To determine subglacial topography and internal features of the Fourcade Glacier on King George Island in Antarctica, helicopter-borne and ground-towed ground-penetrating radar (GPR) data were recorded along four profiles in November 2006. Signature deconvolution, f - k migration velocity analysis, and finite-difference depth migration applied to the mixed-phase, single-channel, ground-towed data, were effective in increasing vertical resolution, obtaining the velocity function, and yielding clear depth images, respectively. For the helicopter-borne GPR, migration velocities were obtained as root-mean-squared velocities in a two-layer model of air and ice. The radar sections show rugged subglacial topography, englacial sliding surfaces, and localised scattering noise. The maximum depth to the basement is over 79 m in the subglacial valley adjacent to the south-eastern slope of the divide ridge between Fourcade and Moczydlowski Glaciers. In the ground-towed profile, we interpret a complicated conduit above possible basal water and other isolated cavities, which are a few metres wide. Near the terminus, the GPR profiles image sliding surfaces, fractures, and faults that will contribute to the tidewater calving mechanism forming icebergs in Potter Cove.

Key words: Fourcade Glaciers, helicopter-borne and ground-towed GPR, internal features, subglacial topography.

Introduction

We report here on the results of helicopter-borne and ground-towed ground-penetrating radar (GPR) surveys of the Fourcade Glacier on King George Island (KGI, Figure 1). KGI, which lies at the northern tip of the Antarctic Peninsula, is one of the most sensitive areas to global warming. The ice cap of KGI lost 65 km² during the period of 1956–2000 (Simões et al., 2004). Glacier flow is controlled by many factors including temperature, subglacial topography, basal water, and physical properties of the ice. Because the wavelengths of radio waves are relatively short and the attenuation of their energy is small in ice, GPR is a powerful tool for various glaciological studies.

As a part of the ‘Glaciology of the South Shetland’ program supported by the Scientific Committee on Antarctic Research, four radar surveys were conducted on KGI to reveal ice thickness and internal structures of the ice caps during the periods of 1995–1996, 1997–1998, and 1999–2000. The radar surveys were conducted along the main divide that bisects the ice caps of the Arctowski icefield, across the Warszawa icefield (Macheret et al., 1997; Pfender, 1999), and in an upper non-crevassed area of the Lange Glacier (Macheret and Moskalovsky, 1999; Travassos and Simões, 2004). Those surveys used ground-based radio echo sounding systems and commercially developed GPR systems, which are used primarily for penetrating rock and soil. A thickness of 308 m was measured on the Lange Glacier near the ice divide that bisects the Arctowski Dome (Macheret and Moskalovsky, 1999). The maximum measured thickness of the ice on KGI was 395 m (Simões et al., 2004).

To determine subglacial topography in the western ablation area of the Fourcade Glacier on KGI, we recorded helicopter-borne GPR data along three profiles in November 2006 (Figure 1). To examine internal structures of the temperate ice

body in detail, we also recorded ground-towed GPR data. The ground-towed GPR data were analysed with shallow seismic data by Kim et al. (2010). In this paper, we briefly describe our acquisition parameters, discuss processing techniques, and interpret englacial and subglacial features using the radar images from both the helicopter-borne and ground-towed GPR data.

Data acquisition

In late November 2006, we acquired GPR data along four profiles in the western part of Fourcade Glacier, which is located between the King Sejong station of Korea and the Teniente Jubany station of Argentina (Figure 1; Table 1). KGI is a volcanic island but without active volcanism. Near the south-west end of Profile S1, bedrock of Palaeogene lapilli tuff is exposed. Near the north-west ends of Profiles A2 and A3, the outcrops are dark grey to greenish basalt and andesite of Palaeocene to Eocene age (Lee et al., 2002).

The 470-m ground-towed profile, S1, and the 1243-m helicopter-borne profile, A1, are approximately perpendicular to the maximum slope of the ice surface in the region of the outlet glacier. The north-east end of Profile A1 is near the divide between the Fourcade and Moczydlowski glacier catchments. The north-west end of the 1219-m helicopter-borne profile A2 is near the north-east end of a dividing ridge that extends east-north-east for ~1 km from Noel Hill at the south-west end of that ridge. The north-west end of the 1373-m helicopter-borne profile A3 is near the col between the ridges at the north-east and north-west ends of Profiles A1 and A2, respectively. Profiles A2 and A3 intersect Profile S1 and trend down the slope of the glacier’s surface towards the sea where they traverse the glacier’s terminus (Figure 1). Highly fractured ice and ice cliffs

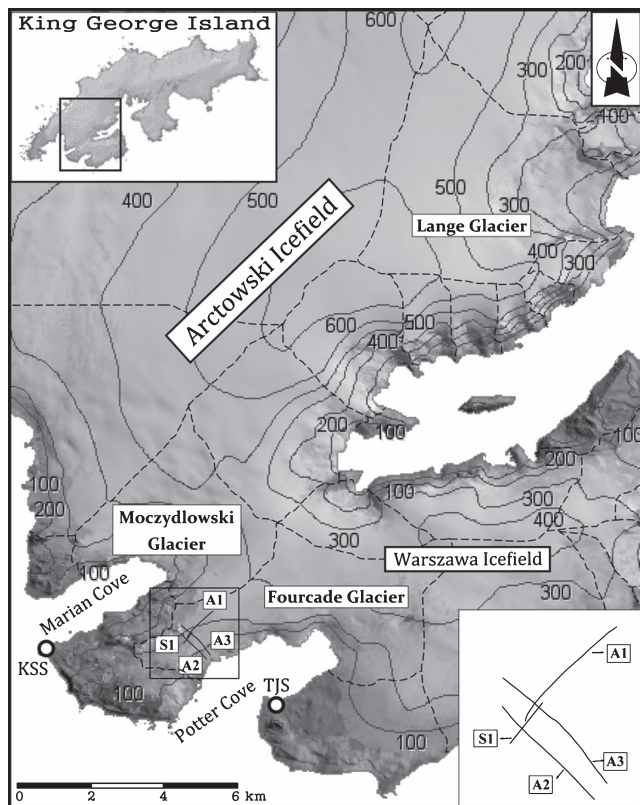


Fig. 1. Map of the western part of Fourcade Glacier showing locations of three helicopter-borne ground-penetrating radar (GPR) profiles, A1–A3, and one ground-towed GPR profile, S1. The surface elevation contours are at 100-m intervals. Catchment boundaries (dashed line) of glaciers, the King Sejong station (KSS), and the Teniente Jubany station (TJS) are also indicated. When the radar survey was conducted, the glacier/sea boundary along Profiles A2 and A3 were 35 and 100 m landward, respectively, from the shoreline depicted on this satellite map of Braun et al. (2004).

with an average height of 35 m at the terminus prevented easy and safe access by ground-towed GPR.

In Profiles A1–A3, the helicopter flew above the ice surface at an average height of 11.9 m guided by a GPS navigation system (Table 1). During the low-altitude helicopter-borne survey, GPS signals were also recorded on the ground in order to post-process the differential GPS data. We used a RAMAC/GPR control unit full-range system and the 100-MHz shielded GPR antenna of Malå Geoscience. The antenna with a fixed transmitter-receiver distance of 0.5 m was mounted between the skids of the helicopter (Figure 2). The transmitter and receiver were oriented perpendicular to the survey direction for operation in the transverse electric mode. A 10-ns radar pulse was generated at 35-ms intervals. The data were digitally recorded at a sampling frequency of 966 MHz for 3700 ns without vertical stacking. Average flight speeds of 12.3 to 23.1 m/s yielded average trace spacings of 1.3 to 2.1 m (Table 1). The helicopter-borne radar data were contaminated by many diffractions at and near the rough

ice surface and by helicopter-generated electromagnetic noise due to imperfect shielding. Although a lower frequency source might have provided better data, the available 50-MHz system was unshielded and therefore unsuitable to the helicopter-borne survey.

The 470-m ground-towed profile S1 traversed a relatively flat ice field covered by a snow layer several centimetres thick. This area provided easy and safe access as well as favourable data conditions with high signal-to-noise (S/N) ratios. To locate GPR stations, survey flags were placed on the ice surface at a 10-m interval. The relative locations and elevations of the flags were then measured with a laser-surveying instrument having a distance resolution of ~ 3 mm/km. The maximum difference in elevation was less than 30 m along the profile. The absolute locations of both ends of the profile were determined with a portable GPS unit. To record the ground-towed GPR data, we used the same control unit as that used for the helicopter-borne survey and a 50-MHz cable-type unshielded antenna of Malå Geoscience.

For simplicity, we ignore the complicated radiation of GPR energy, which depends strongly on the antenna arrangement and the electrical properties of nearby materials. Assuming a constant velocity of 168 m/ μ s in ice (Glen and Paren, 1975), the vertical resolution based on the quarter wavelength criterion and the radius of the first Fresnel zone at 50 m depth are ~ 0.8 m and 4.6 m, respectively. The unshielded antenna, with a fixed transmitter-receiver distance of 4.0 m, generated 20-ns radar pulses, which were recorded in the stream mode at a temporal sampling frequency of 504 MHz. At the walking speed of 2.6 m/s, a horizontal sample rate of 7.7 traces per metre was obtained with four-fold vertical stack.

Data processing

Figure 3 shows the processing sequence that was applied on a personal computer using commercial software. The recorded data were first reformatted to allow processing with the software.

Helicopter-borne data

The absolute location and elevation of each trace were first obtained from the GPS data and then posted on the 1:100 000-scale satellite image map (Braun et al., 2004). Following trace editing and removal of DC components, amplitude attenuation due to geometric spreading was corrected by a programmed gain control. Although the S/N ratio was considerably lowered by the strong reflectivity of the air/ice boundary, vertical stack was not applied in order to preserve dipping events. After removal of ice-coupled radar signatures, a Karhunen-Loeve filter (Jones and Levy, 1987) was applied to enhance S/N ratios by reconstructing with only the first four significant characteristic components. A frequency filter further attenuated ambient noise. Since frequency components of noise varied from profile to profile, the pass band was carefully chosen for each profile separately. Frequency bandwidths of 125–185, 110–190, and 125–185 MHz were chosen for Profiles A1, A2, and A3, respectively. Due to low

Table 1. Ground-penetrating radar acquisition parameters.

Profile	Type	Antenna frequency (MHz)	Length (m)	Height (m)	Average speed (m/s)	Approx. trace interval (m)	Vertical stack
A1	Helicopter-borne	100	1243	12.1	12.3	1.27	1
A2	Helicopter-borne	100	1219	17.2	23.1	2.07	1
A3	Helicopter-borne	100	1373	7.0	14.7	1.40	1
S1	Ground-towed	50	470	0.0	2.6	0.13	4



Fig. 2. The shielded 100-MHz ground-penetrating radar unit mounted between the skids of a helicopter in the broadside transverse electric antenna arrangement. Using this unit, a 10-ns radar pulse was generated at 35-ms intervals and received for 3700 ns at each shot point along Profiles A1–A3 across portions of the Fourcade Glacier.

S/N ratios, deconvolution was not applied to the helicopter-borne data.

Since diffraction hyperbolas in the helicopter-borne data were not clearly imaged as in the ground-towed data, migration velocities were obtained as root-mean-squared (RMS) velocities, v_{rms} , in a two-layer model of air and ice with electromagnetic wave velocities of 300 and 153 m/ μ s, respectively. This velocity in ice was obtained from analysis of the ground-towed data, which we will describe later. Using the computed RMS velocities, 2D depth migration was applied based on a finite difference approximation of the scalar wave equation (Claerbout, 1985). This migration used a depth increment of 0.1 m and a maximum dip of 65 degrees. In order to remove low frequencies induced by this process, post-migration frequency filters were applied with the same bandwidths as in pre-migration filtering. Finally, static shifts were applied to the migrated data to compensate variation in flying-height and to adjust their altitudes to the reference elevation based on the surface topography from the satellite image map (Figure 4). Near the south-east ends of Profiles A2 and A3 (Figure 4b and c), a near-vertical ice cliff is imaged. The difference between the upper surface of the ice cliff and the sea-surface was in agreement with the mapped height of the ice cliff.

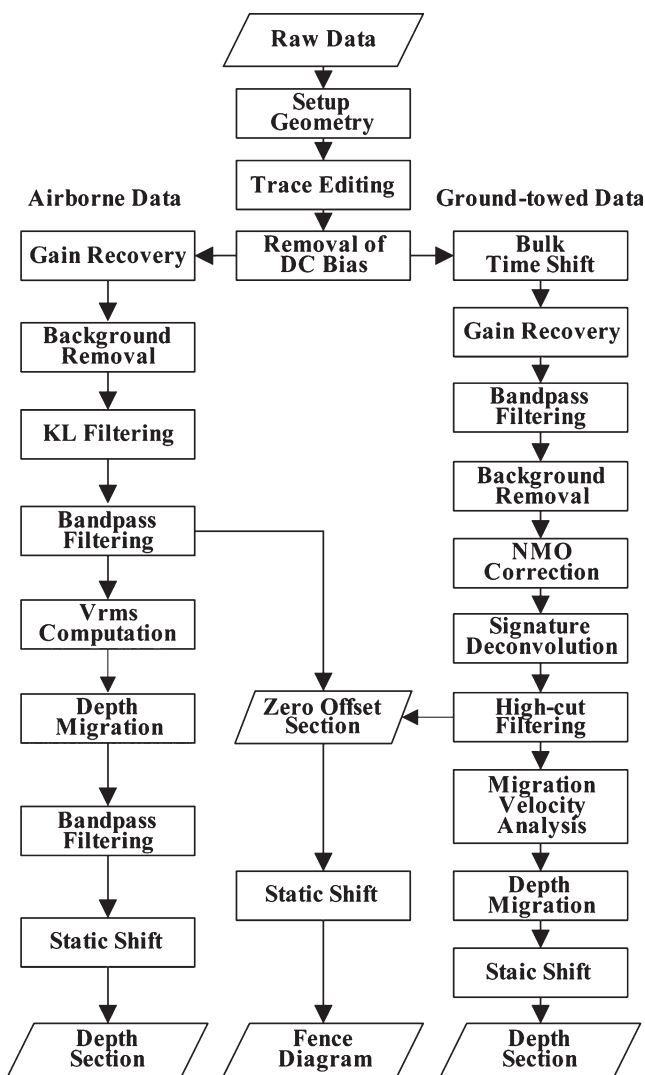


Fig. 3. Flowchart of the processing sequences for helicopter-borne and ground-towed ground-penetrating radar data. NMO, normal moveout.

Ground-towed data

Similar preprocessing was applied to the ground-towed data (Figure 3). After the location and elevation for each trace were determined, trace editing and removal of DC components were applied. Bulk time shifts of 51.0 ns were then applied, geometric spreading was compensated by a programmed gain control, and a zero-phase 25 to 80-MHz bandpass filter was applied to attenuate high- and low-frequency noise. Subtracting the average signal in a 0 to 300 ns time window for profile distances of 110 to 470 m attenuated ice-coupled source signatures. Then normal moveout corrections were applied for the constant source-receiver offset of 4.0 m (Figure 5a). The reflection from the base of the ice is nearly at the surface on the south-west end of the profile and it deepens to ~760 ns corresponding to an ice thickness of 60 m near the north-east end.

Strong scattering noise from within the glacier was recorded in the profile distance range 260–370 m of Profile S1. The helicopter-borne Profile A1 shows less scattering in this region (Figures 1 and 4a). The ground-towed GPR energy may more readily be transmitted away from the normal to the ice surface with consequent greater effect of sideswipe from englacial and subglacial reflectors and diffracting irregularities. For helicopter-borne GPR data, however, refraction at the air/ice interface directs the transmitted energy more towards the normal to the ice surface as it penetrates the ice.

In order to increase vertical resolution, optimum Wiener filters have been applied to radar data (Moran et al., 2000). Due to the mixed-phase nature of GPR signals, however, commonly used deconvolution algorithms based on the minimum-phase assumption often yield undesirable results (Yilmaz, 1987). Therefore, we employed a deterministic method (Carroll, 1972; Ziolkowski, 1991) to deconvolve source signatures. Due to the non-stationarity and the coupling with ice of radar signatures, we did not obtain the radar signals by direct measurement in the air (Xia et al., 2004) but extracted these from signals reflected from the base of the ice (Kim et al., 2006) assuming that any basal water is thin or else absent. To get an average signature for the deconvolution, reflected radar signals from the basement were picked, time-shifted, and stacked where

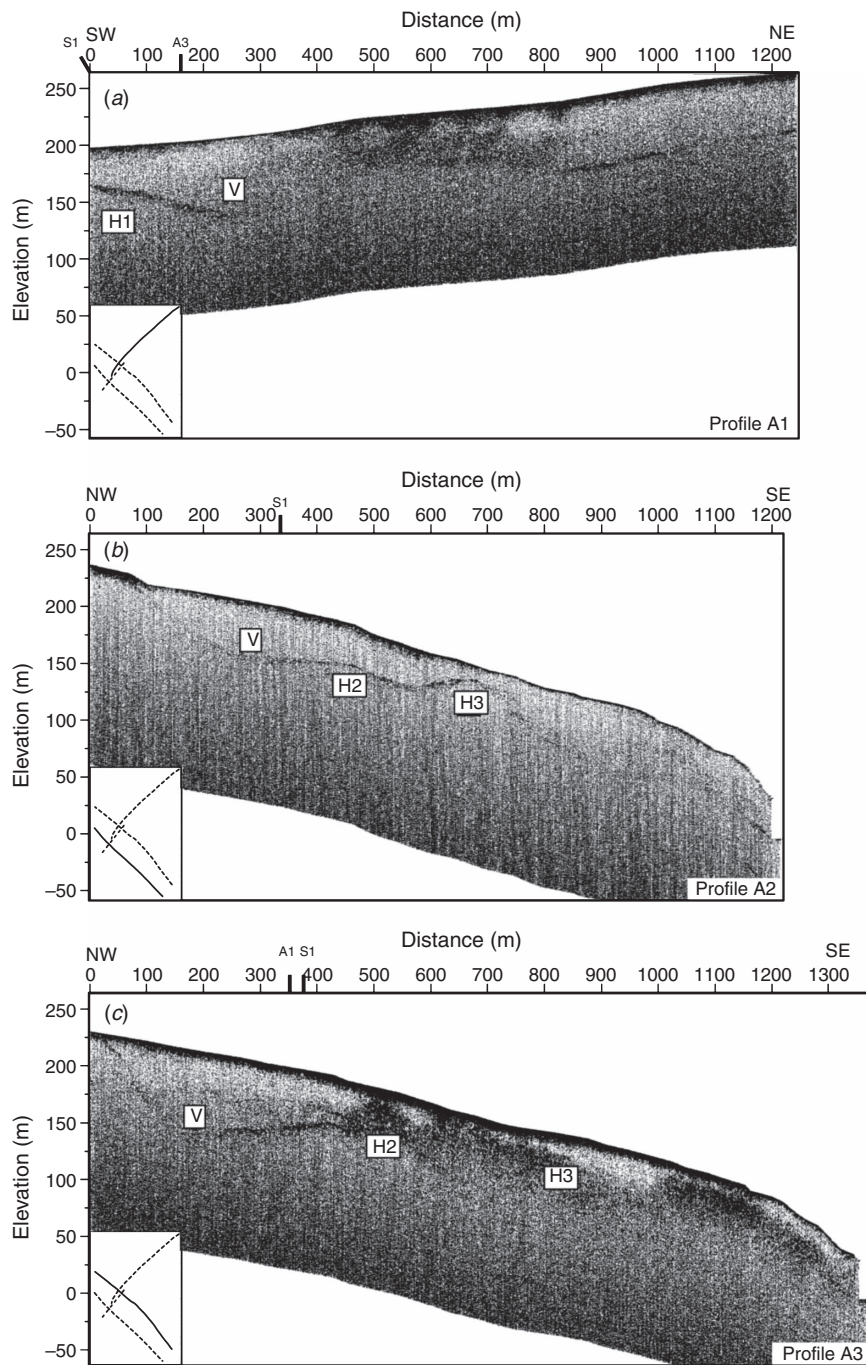


Fig. 4. Depth-migrated sections for Profiles (a) A1, (b) A2, and (c) A3. A distinct subglacial valley (V) and topographic highs (H1–H3) are imaged. The vertical exaggeration is 2 : 1. Line ties are indicated on top of each GPR section. The inset maps show the relative locations of the profiles.

S/N ratios are relatively high (i.e. in the distance range of 85–160 m). For attenuation of high-frequency noise, a high-cut filter was applied to the deconvolved data with a corner frequency of 200 MHz (Figure 5b). The deconvolution successfully compressed the source signatures to increase temporal resolution and attenuated reverberations.

The propagation velocity of radar signals can be measured in the field in several ways (Robin, 1975; Jezek and Roeloffs, 1983; Murray et al., 2000). Where no drill hole is available, velocity analysis of common midpoint data or wide-angle reflections may be used (Macheret et al., 1993). To minimise acquisition time, however, no attempt was made to use reflected radar signals in the present survey. Instead, we used the constant-velocity migration

method in the frequency-wavenumber (f - k) domain based on the Stolt algorithm (Stolt, 1978) to derive the spatially varying velocity function from diffraction events. For the migration process, a stretch factor of 1.0, a maximum frequency to migrate of 300 MHz, and a taper width of five traces were chosen. The medium velocities were analysed for 112 such events using migration velocities in the range of 100 to 188 m/ μ s at a 1 m/ μ s interval. Proper velocities collapsed these events to points while under-migration using erroneously low velocities yielded ‘frowns’ and over-migration using erroneously high velocities yielded ‘smiles’. A smoothly varying migration velocity was then derived as a function of time and profile distance from the analysis of individual

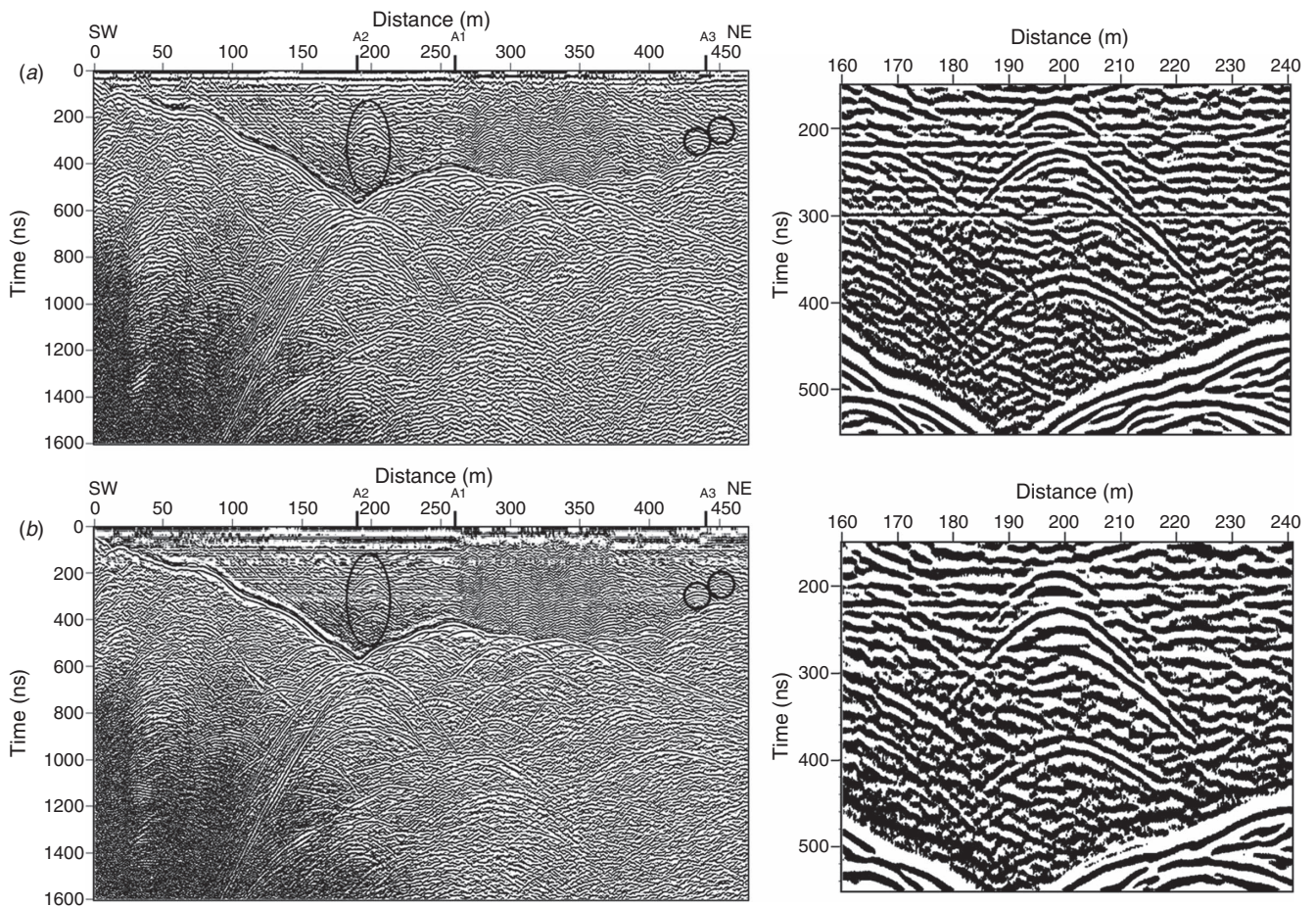


Fig. 5. Normal moveout-corrected radar sections of Profile S1 (a) before and (b) after signature deconvolution. On the right, expanded portions of these sections for the profile distance range of 160–240 m show that the deconvolution successfully attenuated reverberations and compressed the mixed-phase source signatures to increase temporal resolution. Automatic gain control with a 10-ns window was applied to the radar sections for display purpose only. Diffractions possibly generated by edges of cavities (open ellipse and circles) are collapsed in the migrated section (Figure 7).

diffractions (Figure 6). The average velocity near the base of the glacier is ~ 153 m/ μ s.

Using the smoothed migration velocity function, 2D depth migration was applied to the high-cut filtered data with the same parameters for the helicopter-borne data. For the frequency of 50 MHz and the velocity of 153 m/ μ s, the horizontal resolution after migration with an aperture width of 200 m is ~ 1.2 m at a 25 m depth assuming the far-field and plane-wave approximation (Chen and Schuster, 1999). Finally, elevation shifts were applied to the migrated database on the digital topography map (Braun et al., 2004). The elevation-corrected migration section shows that dipping reflectors were moved to their correct positions, most diffractions were effectively collapsed, and the horizontal resolution was thereby improved (Figure 7).

Fence diagram

To envisage 3D features of englacial structures and subglacial topography of the western part of the Fourcade Glacier, the filtered pre-migration data in Figures 4 and 5 were tied at every crossing point. Based on the surface topography from the satellite image map, differences in elevation between each trace and a flat datum were converted to two-way time shifts using the speed of electromagnetic waves in the air, 300 m/ μ s. After application of such time shifts, a fence diagram was constructed using both ground-towed and helicopter-borne GPR data (Figure 8). This simple approach of removing

elevation effect causes misties between helicopter-borne and ground-towed GPR data for dipping events by the amount of the flight height multiplied by tangent of the incidence angle. However, we assumed a flat air/ice interface and zero incidence angles for the radar beam.

Analysis and interpretation

Subglacial topography and ice thickness

The western part of the Fourcade Glacier is characterised by rugged subglacial topography of buried valleys and ridges (Figure 8). Subtle effects of the buried topography on the configuration of the ice surface may be indicated in the satellite image where the low angle of illumination by the sun has emphasised changes in surface elevation (Figure 1). In Profile A3 the depth to the base of the glacier is over 79 m at a profile distance of 185 m (Figure 4c). Subglacial valleys dissect the south-eastern slope of the divide ridge between the Fourcade and Moczydlowski Glaciers in the north-west; however, the actual courses of these valleys cannot be traced using the sparse coverage provided by the four GPR profiles. Near the divide ridge above the valleys, the apparent dip of the slope of the sub-ice terrain is $\sim 19^\circ$ SE in Profile A2 (Figure 4b) and 30° SE in Profile A3 (Figure 4c). Given the slopes determined by radar, separate valleys are indicated on Profiles A2 and A3. The definition of the valleys is enhanced by migration. For example, a V-shaped image of one valley beneath profile S1 is shown

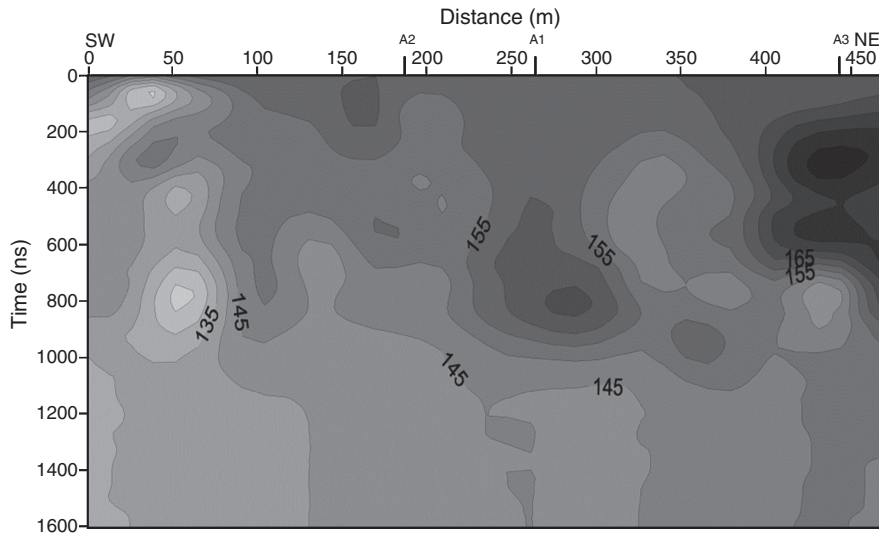


Fig. 6. The smoothed velocity function from the migration velocity analysis. Relatively low velocities in the ice body are in the distance ranges of 190–220 m and 320–350 m, where drainage structures, fractures, inclusions of water-filled voids, or debris may exist in the ice. The average velocity along the basement surface is ~ 153 m/ μ s.

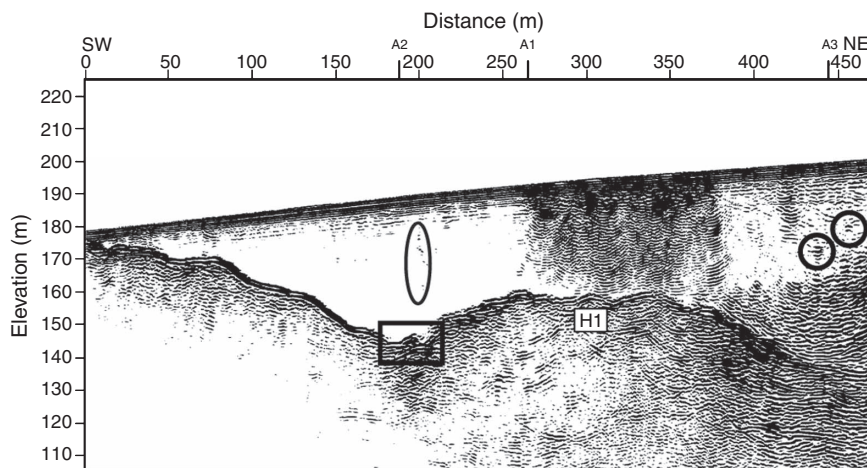


Fig. 7. Elevation-corrected depth-migration section of Profile S1 after high-cut filtering. Compared with unmigrated data (Figure 5), dipping reflectors were moved to their correct positions and most diffractions were collapsed efficiently. Strong scattering noise is recorded in the ice body in the distance ranges of 260–370 m. Flat events of basal water reflections (box) and cavities (ellipse and circles) are highlighted.

before migration (Figure 5), while a broad valley is imaged after migration (Figure 7).

Profiles S1 and A1 lie near the base of the partially buried bedrock ridge that outcrops near the north-west ends of Profiles A2 and A3. That is, in Profiles A2 and A3 the apparent dips of the bedrock surface are significantly less to the south-east than to the north-west of Profile S1. In Profiles S1 and A1, a hummocky high lies between the valley at the intersection of Profiles S1 and A2 near a profile distance of 190 m and the valley near the north-east end of Profile S1. This high area is likely a bedrock feature; although it is possible that a medial moraine has been deposited above or down slope of such a high between the valleys defined on Profiles A2 and A3. Numerous diffractions in the GPR images may be associated with the hummocky nature of the terrain and the inhomogeneity of weathered volcanic rocks or moraine deposits.

The ice is thickest above a valley, or valleys, near the intersection of Profiles A1 and A3. The estimated thickness is 79 m at the 185-m location on Profile A3 (Figure 4c) and 76 m at the 250-m location on Profile A1 (Figure 4a). Perhaps in response to recent warming, the termini of Profiles A2 and A3 at the glacier-sea boundary have moved landward by 35 and 100 m, respectively.

Englacial features

In the upper several metres of all the sections with varying thickness, sub-horizontal scattering noise is strongly recorded. Variation in water content, due to superficial melting during the summer, is a probable cause for much of this scattering noise.

At distances of 70, 470, and 995 m of Profile A2 (Figure 4b) and distances of 425 and 1155 m of Profile A3 (Figure 4c), the

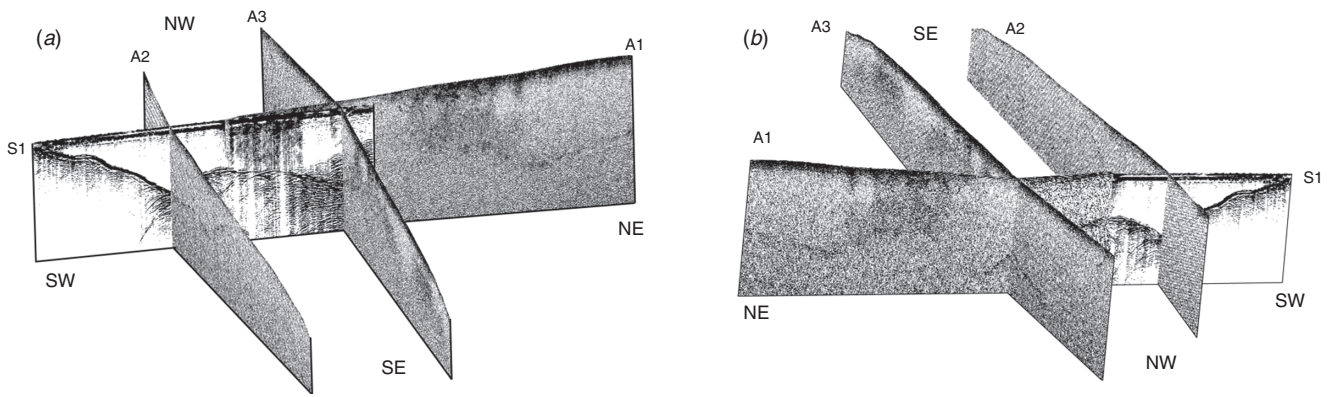


Fig. 8. Fence diagrams of four unmigrated ground-penetrating radar profiles, A1–A3 and S1. 3D features of englacial structures and the base of glacier are shown as viewed from above and ESE or WNW of the profiles in diagrams (a) and (b), respectively.

slope of the ice surface changes abruptly and low-angle sliding surfaces may be imaged beneath the thin snow layer. These changes at the surface result from changes in slope of the ice-basement surface that alter the flow of the glacier. Near the terminus, many faults, fractures, and sliding surfaces with various dips are interpreted in Profiles A2 and A3 (Figure 9). Some of these serve as important drainage passages of englacial melt water. These structures may also contribute to ablation near the terminus and to the calving of icebergs into Potter Cove (Figure 1). The sub-glacial shore dips steeply into Potter Cove, as is indicated by the radar image of that shore and the form of the glacier’s surface. The glacier presently remains grounded here, as it does not extend far enough into deeper waters of the cove to form an ice shelf.

Exceptionally strong diffractions occur in the distance ranges of 260–370 m of Profile S1 (Figure 7), 410–840 m of Profile A1 (Figure 4a), and 450–820 m of Profile A3 (Figure 4c). Associated linear reflections, or perhaps limbs of edge diffractions, with dominant apparent dips of 30–45°SW in Profiles A1 and S1 and 25–40°NW in Profile A3, are also imaged in these regions. Radar scattering was probably enhanced here by local changes in the amount of interglacial water. Water within fractures and greater

water content of ice adjacent to such fractures and faults is likely. In the case of Profile S1, this region of strong scattering correlates with a decrease in the interpreted radar velocity derived from the migration velocities necessary to collapse these diffractions (Figure 6). The decreased radar velocity has also been associated with increased water content of the glacier. A decrease in seismic P-wave velocity was also interpreted in this portion of Profile S1 using seismic tomography (Kim et al., 2010).

In the distance range 180–220 m of Profile S1, strong hyperbolic diffractions are indicated in a vertical sequence through much of the glacier’s thickness (Figure 5). After migration to collapse these diffractions, a near vertical series of strong reflection events were revealed in the approximate depth range of 14–30 m (Figure 7). These features may indicate reverberations of radar energy within englacial voids. However, we tentatively interpret these discrete features as cavities ~1.4 m wide in the ice since their apices are not distributed along a vertical line. This dimension is approximately twice the horizontal resolution limit in the shallower part of the section. These possible cavities may be connected as a downward-trending spiral such as has been

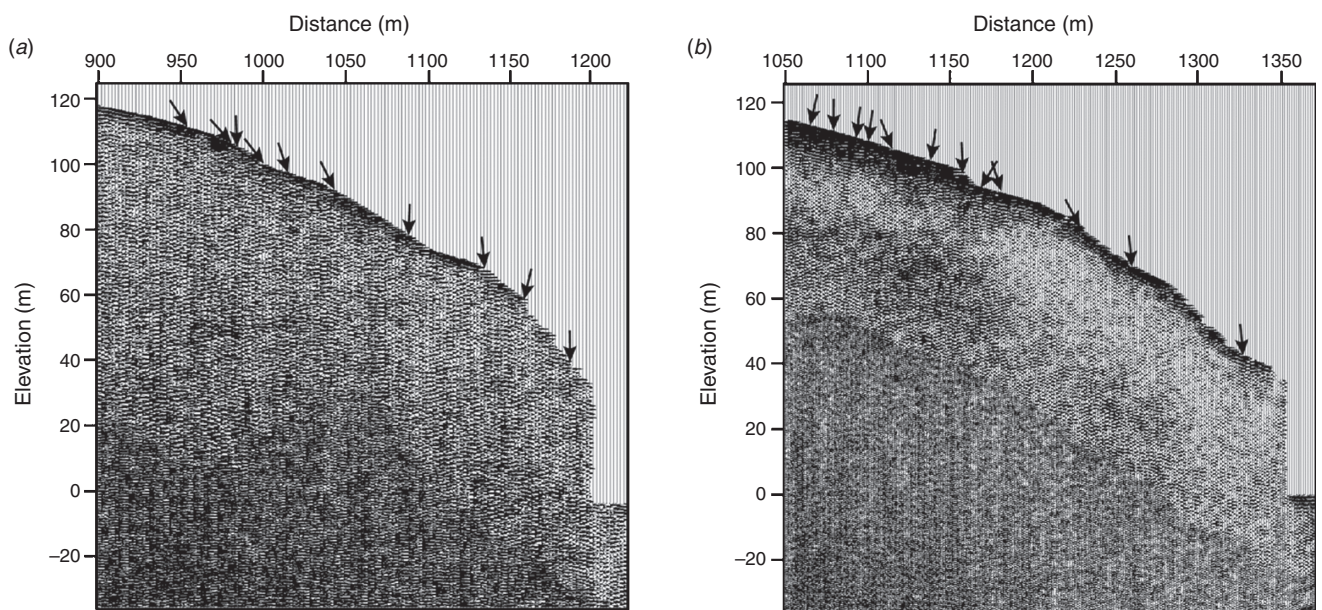


Fig. 9. Enlarged sections near the termini of helicopter-borne ground-penetrating radar Profiles (a) A2 and (b) A3. A series of sub-linear reflection events of faults, fractures, and sliding surfaces are indicated on the ice surface with arrows.

described elsewhere by Majjala et al. (1998). One diffraction-limited reflection event at a depth of 28 m (reflection time of 390 ns) is imaged beneath the vertical stack of shallower anomalies (Figure 5). It is possible that this feature is associated with the shallower events above it. Thus conduits for water may extend from the surface of the glacier to the base of the glacier in this region. In the deepest part of the valley beneath this interpreted series of cavities sub-horizontal reflectors at the base of the ice at depths of 46 to 47 m may be generated by an ice-water interface at the base of the glacier (Figure 7). Other strong isolated diffractions are imaged at 292 and 237 ns near the north-east end of Profile S1 (Figure 5). After migration (Figure 7) these diffraction events are collapsed and short reflection events are revealed with lateral extents of ~1.7 and 2.1 m at depths of 21 and 27 m, respectively. These events may be generated by cavities in the colder ice of this region beneath Profile S1.

Widely spread scattering noise is prevalent 20–40 m below the ice surface in the helicopter-borne profiles (Figure 4). This type of scattering is probably caused by warm ice under the refrozen cold ice layer, which is typical in polythermal glaciers (Dowdeswell and Evans, 2004; Irvine-Fynn et al., 2006). In Profile S1, relatively low shear-wave velocities in the warm ice layer were derived from seismic surface waves (Kim et al., 2010). These lower velocities are indicative of significantly lower rigidity in this layer.

Conclusions

From our helicopter-borne and ground-towed GPR surveys in the western part of Fourcade Glacier on KGI, we conclude the following:

Using the source signature extracted from reflection signals, deterministic deconvolution was successfully applied to increase vertical resolution of the mixed-phase data. The migration velocity analysis was an effective tool for the horizontally and vertically varying velocity field from the single-channel ground-towed radar data. Finally, finite-difference depth migration yielded clear depth images of both englacial structures and subglacial topography. Helicopter-borne GPR data were generally much poorer than the ground-towed data; however, the helicopter-borne method did allow access to areas otherwise inaccessible and it provided much quicker surveying with useful definition of sub-glacial topography.

The western part of the Fourcade Glacier is characterised by rugged subglacial topography of buried valleys and ridges. The maximum ice thickness is over 79 m in the subglacial valley adjacent to the south-eastern slope of the divide ridge between the Fourcade and Moczydlowski Glaciers. Faults, fractures, and sliding surfaces with various dips identified near the terminus serve as important drainage passages of melt water. These englacial structures may also contribute to the calving mechanism forming icebergs in Potter Cove. In addition, several distinct concave sliding surfaces and englacial hollows of a near-vertical conduit and an isolated cavity were identified on the GPR sections.

Strong diffraction or scattering of the radar signal varies according to the water content of the ice and in some cases it may indicate water-filled cavities within the ice as well as variations of water content near fractures or faults within the ice. Where the water content of the Fourcade glacier is greater, the radar-wave velocity is lowered. P- and S-wave velocities, which are derived from a seismic survey conducted in a survey coincident to the ground towed radar Profile S1 (Kim et al., 2010), also decrease with increasing the water content of the

glacier. GPR generally provided a better definition of the sub-glacier topography; however, the synergetic interpretation of GPR and seismic survey data helps to confirm interpretations of the glacier's water content based on GPR velocities.

Acknowledgments

This work was supported through the Korea Science and Engineering Foundation (KOSEF) grant R01-2007-000-20194-0 by the Ministry of Science and Technology (MOST) and through the Grant PE09020 by the Korea Polar Research Institute (KOPRI). We thank Drs. Jong Ik Lee and Young Keun Jin at the KOPRI who supported us in many aspects of the fieldwork. We are also grateful to Dr Moon Young Choe, the 19th commander of King Sejong station, and his over-winter crews who allowed us to use all facilities at the station, provided transportation for the fieldwork, and otherwise assisted our fieldwork. We also thank two Chilean helicopter pilots at Presidente Eduardo Frei Montalva station for their careful flight above the glacier. Finally we appreciate Dr Raymond M. René at René Geophysics and Professor Hoonyol Lee at Kangwon National University for their helpful discussions and suggestions during the progress of this work.

References

- Braun, M., Simões, J. C., Vogt, S., Bremer, U. F., Saurer, H., Aquino, F. E., and Ferron, F. A., 2004, A new satellite image map for King George Island, Antarctica: *Pesquisa Antarctica Brasileira*, **4**, 199–203.
- Carroll, P., 1972, Signature deconvolution for marine seismic reflection surveys: *CSEG Journal*, **8**, 41–53.
- Chen, J., and Schuster, G. T., 1999, Resolution limits of migration images: *Geophysics*, **64**, 1046–1053. doi:10.1190/1.1444612
- Claerbout, J. F., 1985, *Imaging the earth's interior*: Blackwell Scientific Publications.
- Dowdeswell, J. A., and Evans, S., 2004, Investigations of the form and flow of ice sheets and glaciers using radio-echo sounding: *Reports on Progress in Physics*, **67**, 1821–1861. doi:10.1088/0034-4885/67/10/R03
- Glen, J. W., and Paren, J. G., 1975, The electrical properties of snow and ice: *Journal of Glaciology*, **15**, 15–37.
- Irvine-Fynn, T. D., Moorman, B. J., Williams, J. L. M., and Water, F. S. A., 2006, Seasonal changes in ground-penetrating radar signature observed at a polythermal glacier, Bylot Island, Canada: *Earth Surface Processes and Landforms*, **31**, 892–909. doi:10.1002/esp.1299
- Jezek, K. C., and Roeloffs, E. A., 1983, Measurements of radar wave speeds in polar glaciers using down-hole radar target technique: *Cold Regions Science and Technology*, **8**, 199–208. doi:10.1016/0165-232X(83)90010-1
- Jones, I. F., and Levy, S., 1987, Signal-to-noise ratio enhancement in multichannel seismic data via the Karhunen-Loeve transform: *Geophysical Prospecting*, **35**, 12–32. doi:10.1111/j.1365-2478.1987.tb00800.x
- Kim, K. Y., Hong, M. H., Shon, H., and Lee, J. H., 2006, Enhancement of vertical resolution of GPR data through signature deconvolution: *Journal of Korean Geophysicists Society*, **9**, 1–6.
- Kim, K. Y., Lee, J., Hong, M. H., Hong, J. K., Jin, Y. G., and Shon, H., 2010, Seismic and Radar Investigations of the Fourcade Glacier on King George Island, Antarctica: *Polar Research*.
- Lee, J. I., Hur, S. D., Yoo, C. M., Yeo, J. P., Kim, H., et al., 2002, *Geologic map of Barton and Weaver Peninsulas, King George Island, Antarctica (1:10 000)*: Korea Ocean Research and Development Institute, Ansan.
- Macheret, Y. Y., and Moskalovsky, M. Y., 1999, Study of Lange Glacier on King George Island, Antarctica: *Annals of Glaciology*, **29**, 202–206. doi:10.3189/172756499781820941
- Macheret, Y. Y., Moskalovsky, M. Y., and Vasilenko, E. V., 1993, Velocity of radio waves in glaciers as an indicator of their hydrothermal state, structure and regime: *Journal of Glaciology*, **39**, 373–384.
- Macheret, Y. Y., Moskalovsky, M. Y., Simões, J. C., and Ladouch, L., 1997, Radio-echo sounding of King George Island ice cap, South Shetland Islands, Antarctica: *Master Glyatsiol Issled*, **83**, 121–128.
- Majjala, P., Moore, J. C., Hjelt, S.-E., Palli, A., and Sinisalo, A., 1998, GPR investigation of glaciers and sea ice in the Scandinavian Arctic: *GPR98-7th International Conference on Ground-Penetrating Radar Proceedings*, 143–148.

- Moran, M. L., Greenfield, G. J., Arcone, S. A., and Delaney, A. J., 2000, Delineation of a complexly dipping temperate glacier bed using short pulse radar arrays: *Journal of Glaciology*, **46**, 274–286. doi:10.3189/172756500781832882
- Murray, T., Stuart, G. W., Fry, M., Gamble, N. H., and Crabtree, M. D., 2000, Englacial water distribution in a temperate glacier from surface and borehole radar velocity analysis: *Journal of Glaciology*, **46**, 389–398. doi:10.3189/172756500781833188
- Pfender, M., 1999, *Topographie und Glazialhydrologie von King George Island, Antarktis*: Münster, Westfälischen Wilhelms-Universität Münster (Diplomarbeit im Fach Geophysik).
- Robin, G. de Q., 1975, Velocity of radio waves in ice by means of a bore-hole interferometric technique: *Journal of Glaciology*, **15**, 151–159.
- Simões, J. C., Gofmann, H., Delmas, R. J., and Moskalevsky, M. Y., 2004, Glaciological research in King George Island: Missions and developments in the 1990s: *Pesquisa Antarctica Brasileira*, **4**, 1–4.
- Stolt, R. H., 1978, Migration by Fourier transform: *Geophysics*, **43**, 23–48. doi:10.1190/1.1440826
- Travassos, J. M., and Simões, J. C., 2004, High-resolution radar mapping of internal layers of a subpolar ice cap, King George Island, Antarctica: *Pesquisa Antarctica Brasileira*, **4**, 9–23.
- Xia, J., Franseen, E. K., Miller, R. D., and Weis, T. V., 2004, Application of deterministic deconvolution of ground-penetrating radar data in a study of carbonate strata: *Journal of Applied Geophysics*, **56**, 213–229.
- Yilmaz, Ö., 1987, *Seismic data processing*: Society of Exploration Geophysicists, Tulsa.
- Ziolkowski, A., 1991, Why don't we measure seismic signatures?: *Geophysics*, **56**, 190–201. doi:10.1190/1.1443031

Manuscript received 14 November 2008; accepted 6 November 2009.

ヘリボーンと地上牽引のレーダによる南極キングジョージ島のフォーケード氷河の探査

金 基榮¹・李 周漢²・洪 明鎬¹・洪 種國²・孫 浩雄³

1 江原大学校

2 韓国極地研究所

3 培材大学校

要 旨: 南極キングジョージ島のフォーケード氷河下部地形および内部構造を決定するため、2006年12月、ヘリボーンおよび地上牽引により4断面の地中レーダ(GPR)データを記録した。混合位相のシングルチャンネル地上牽引データに対し、シグネチャデコンボリューション、F-Kマイグレーション速度解析、有限差分深度マイグレーションを適用し、それぞれ、垂直分解能の向上、速度関数の取得、明瞭な深度イメージの取得に効果をもたらした。ヘリボーンGPRのために、空気と氷の2層モデルにおけるRMS速度としてマイグレーション速度を取得した。そのレーダ断面は、起伏に富む氷河下部地形や氷河内部のすべり面、局在する散乱ノイズを示している。フォーケード氷河とモチユドロウスキ氷河間にある分水嶺の、南東斜面に隣接した氷河下部の谷地形にて、基盤までの最大深度は79m以上となっている。地上牽引記録断面において、基底水と考えられる部分および独立した空洞の上方に数メートルの幅を有する複雑な流動経路が解釈される。氷河の先端付近では、GPR断面がすべり面や亀裂および断層を示しており、ポッター湾の氷山を生み出す、潮汐による氷山形成メカニズムの解明に貢献する可能性がある。

キーワード: フォーケード氷河とモチユドロウスキ氷河, 地中レーダデータ

남극 킹조지섬 포케이드 빙하의 헬리콥터 및 지상 레이더 탐사

김기영¹, 이주한², 홍명호¹, 홍종국², 손호웅³

1 강원대학교 지구물리학과

2 한국해양연구원 극지연구소

3 배재대학교 건설환경철도공학과

요 약: 남극 킹조지섬 포케이드 빙하의 지면 지형과 내부 모습을 규명하기 위해서 2006년 11월에 4개 조사측선을 따라 헬리콥터 및 지상 레이더(GPR) 탐사를 실시하였다. 혼합위상인 단채널 지상 GPR 자료에 적용한 신호 역대합, f-k 구조보정 속도분석, 유한차분 깊이구조보정 등의 처리과정을 통하여 수직 분해능 향상, 속도함수 추출, 선명한 깊이영상 작성 등을 효과적으로 수행하였다. 헬리콥터 GPR 자료의 경우, 구조보정속도는 공기와 얼음의 2층모델을 가정한 평균제곱근속도로 구하였다. GPR 단면은 울퉁불퉁한 빙저면, 빙하 내부의 미끄러짐면, 운집된 산란잡음 등의 특징적 모습을 보여준다. 기반암까지의 최대 깊이는 포케이드 빙하와 목지들로우스키 빙하 사이의 경계능선 남동사면에 인접한 빙하 골짜기에서 79 m가 넘는다. 빙하 기저수 위에 복잡한 형태의 굴과 수 m의 폭을 갖는 독립된 빈 공간들의 존재를 지상 GPR 자료로부터 해석하였다. 빙하 종단 부근의 GPR 영상은 포토소만의 빙산 형성기작과 관련된 미끄러짐면, 단열, 단층 등의 구조를 보여준다.

주요어: 포케이드 빙하, 헬리콥터 및 지상 GPR, 빙저면 지형, 빙하내부 모습